Lagrangian investigations of velocity gradients in compressible turbulence: lifetime of flow-field topologies

Nishant Parashar[1],†, **Sawan Suman Sinha**[1] **and Balaji Srinivasan**[2]

[1]Department of Applied Mechanics, Indian Institute of Technology Delhi, New Delhi 110016, India

[2]Department of Mechanical Engineering, Indian Institute of Technology Madras, Chennai 600036, India

We perform Lagrangian investigations of the dynamics of velocity gradients in compressible decaying turbulence. Specifically, we examine the evolution of the invariants of the velocity-gradient tensor. We employ well-resolved direct numerical simulations over a range of Mach number along with a Lagrangian particle tracker to examine trajectories of fluid particles in the space of the invariants of the velocity gradient tensor. This allows us to accurately measure the lifetimes of major topologies of compressible turbulence and provide an explanation of why some selective topologies tend to exist longer than the others. Further, the influence of dilatation on the lifetime of various topologies is examined. Finally, we explain why the so-called conditional mean trajectories (CMT) used previously by several researchers fail to predict the lifetime of topologies accurately.

Key words: compressible turbulence, homogeneous turbulence

1. Introduction

Gradients of the velocity field and its dynamics in a turbulent flow influence many important nonlinear turbulence processes like cascade, mixing, intermittency and material element deformation. Thus, examination of the velocity-gradient tensor in canonical turbulent flow fields has been a subject of interest. Various studies have been performed employing experimental measurements (Lüthi, Tsinober & Kinzelbach 2005), direct numerical simulations (DNS) (Ashurst *et al.* 1987*b*) as well as simple autonomous dynamical models (ordinary differential equations) (Vieillefosse 1982; Cantwell 1992) of velocity gradients. The pioneering works done by these authors have been further followed up extensively by several researchers for both incompressible (Ashurst, Chen & Rogers 1987*a*; Girimaji & Pope 1990*a*; Ohkitani 1993; Pumir 1994; Soria *et al.* 1994; Girimaji & Speziale 1995; O'Neill & Soria 2005; Chevillard & Meneveau 2006; da Silva & Pereira 2008; Chevillard & Meneveau 2011) and compressible turbulence (Pirozzoli & Grasso 2004; Suman & Girimaji 2009, 2010, 2012; Wang & Lu 2012; Vaghefi & Madnia 2015; Danish, Sinha & Srinivasan 2016*a*; Parashar *et al.* 2017*a*).

† Email address for correspondence: nishantparashar14@gmail.com

Most DNS or experiment-based studies of turbulent flows have so far been performed using the Eulerian approach. However, it is desirable to investigate flow physics following individual fluid particles (via Lagrangian tracking) as well. Such an investigation is especially required for developing/improving simple dynamical models of velocity gradients like the restricted Euler equation (REE) (Cantwell 1992; Girimaji & Speziale 1995; Meneveau 2011) and the enhanced homogenised Euler equation model of Suman & Girimaji (2009). Such simple models, in turn, can be used for the closure of the Lagrangian probability density function (PDF) method of turbulence (Pope 2002). An apt example of how Lagrangian statistics can reveal more insights into velocity-gradient dynamics is the recent experimental study of Xu, Pumir & Bodenschatz (2011), wherein the authors provided evidence of the so-called 'Pirouette effect'. Even though the vorticity vector had always been expected to align with the largest strain-rate eigenvector, the Eulerian investigations performed by Ashurst *et al.* (1987*b*) revealed a counter-intuitive picture of vorticity aligning most strongly with the intermediate eigenvector of the instantaneous local strain-rate tensor. Xu *et al.* (2011), with their experimental Lagrangian investigations, provided experimental evidence that indeed the vorticity vector dynamically attempts to align with the largest strain-rate eigenvector of an initial reference time. Buxton & Ganapathisubramani (2010) and Bechlars & Sandberg (2017*b*) provide similar insights regarding vorticity–strain alignment tendencies using their Eulerian approach as well.

In incompressible flows, Lagrangian studies using the direct numerical simulation of decaying turbulence have been performed earlier by Yeung & Pope (1989) and Girimaji & Pope (1990*b*). Yeung & Pope (1989) focused on Lagrangian statistics of velocity, acceleration and dissipation. Girimaji & Pope (1990*b*) examined the evolution of material elements in incompressible decaying turbulence. Recently, Xu *et al.* (2011) have complemented their experimental observations of vorticity alignment with the Lagrangian data extracted from DNS of forced isotropic turbulence as well. Chevillard & Meneveau (2011) evaluated the Lagrangian model for the velocity-gradient tensor for its capability in predicting vorticity alignment using Lagrangian data obtained from DNS of forced isotropic turbulent flow. Bhatnagar *et al.* (2016) quantified the persistence time of fluid particles in vorticity-dominated and strain-dominated topologies using Lagrangian data obtained from DNS of isotropic incompressible turbulence.

In compressible turbulence, Lagrangian statistics of velocity gradients have been recently studied by Danish *et al.* (2016*a*) and Parashar *et al.* (2017*a*). While Danish *et al.* (2016*a*) provided first glimpses of compressibility effects on the alignment tendencies of the vorticity vector, Parashar *et al.* (2017*a*) followed it up and made attempts at explaining the observed behaviour in terms of the dynamics of the inertia tensor of fluid particles and the angular momentum of tetrads representing fluid elements. In continuation of our effort to develop deeper insight into the dynamics of small-scale turbulence from a Lagrangian perspective, in this work, we focus on the lifetimes of the flow-field topology and their conversion tendencies in compressible turbulence.

We examine the evolution of flow-field topology in compressible turbulence following the Lagrangian trajectories (LT) of the invariants of the velocity-gradient tensors. Topology can be visualised as the local streamline pattern, observed with respect to a reference frame which is translating with the centre of mass of a local fluid element (Chong, Perry & Cantwell 1990). Topology actually depends on the nature of the eigenvalues of the velocity-gradient tensor (VGT), but can also be readily determined by knowing the three invariants of the VGT (Cantwell & Coles

1983; Chong *et al.* 1990). Flow-field topology can also be used for visualisation of a flow field. Further, topology has been shown to reveal deeper insights into various nonlinear turbulence processes as well (Cantwell 1993; Soria *et al.* 1994). Recently, Danish, Suman & Girimaji (2016b) have attempted to develop models for scalar mixing using topology as a conditioning parameter.

The time spent by fluid particles in different topological states is of significance in raindrop formation (Pinsky & Khain 1997) and the formation of proplanetary disks (Armitage 2010) as well. Traditionally, due to the prohibitive demand of computational resources, the dynamics of the topology has been studied employing an approximate surrogate method called the conditional mean trajectory (CMT). The idea of CMT was proposed by Martín *et al.* (1998), who employed merely a one-time velocity gradient field and computed bin-averaged rates of change of second and third invariants of VGT using the right-hand sides of the evolution equations of the invariants. These averaged rates of change conditioned upon their locations were subsequently used to plot trajectories in the space of VGT invariants. The authors called these trajectories conditional mean trajectories (CMT) and used them as a surrogate approach to study the invariant dynamics. Subsequently, several authors have employed CMTs to investigate various aspects of topology dynamics both for incompressible (Martín *et al.* 1998; Ooi *et al.* 1999; Elsinga & Marusic 2010; Meneveau 2011; Atkinson *et al.* 2012; Zhou *et al.* 2015) and compressible flows (Chu & Lu 2013; Bechlars & Sandberg 2017a). Even though CMTs do provide some useful information about the dynamics of invariants, they remain approximate and merely a surrogate approach in the absence of adequate computational resources (Martín *et al.* 1998). An investigation of the exact Lagrangian dynamics in compressible turbulence must be performed for better insight, if adequate computational resources are available. This is the motivation for our employment of the LTs to investigate the lifetimes of topologies and their conversion tendencies in compressible turbulence.

To address the objectives of this paper, we employ direct numerical simulations of decaying isotropic compressible turbulence over a range of turbulent Mach numbers (0.4–0.8) using computational grids up to 1024^3. The Lagrangian dynamics is obtained using an almost time continuous set of Eulerian flow fields along with a spline-aided Lagrangian particle tracker (more details in §3).

This paper is organised into seven sections. In §2 we present the governing equations. In §3 we provide details of our direct numerical simulations as well as the Lagrangian particle tracker. In §4 we present the governing equations of the velocity-gradient invariants and cast them in a form suitable for our study. In §5 we present our results on lifetimes of various flow topologies existing in compressible turbulence, and further compare our results of CMTs with LTs. We explain the significance and implications of our work in §6. Section 7 concludes the paper with a summary of the main results.

2. Governing equations

The time evolution of a compressible flow field is governed by the following equations:

$$\frac{\partial \rho}{\partial t} + V_k \frac{\partial \rho}{\partial x_k} = -\rho \frac{\partial V_k}{\partial x_k}; \tag{2.1}$$

$$\frac{\partial V_i}{\partial t} + V_k \frac{\partial V_i}{\partial x_k} = -\frac{1}{\rho}\frac{\partial p}{\partial x_i} + \frac{1}{\rho}\frac{\partial \sigma_{ik}}{\partial x_k}; \tag{2.2}$$

$$\frac{\partial T}{\partial t} + V_k \frac{\partial T}{\partial x_k} = -T(n-1)\frac{\partial V_i}{\partial x_i} - \frac{n-1}{\rho R}\frac{\partial q_k}{\partial x_k} + \frac{n-1}{\rho R}\frac{\partial}{\partial x_j}(V_i \sigma_{ji}); \qquad (2.3)$$

$$p = \rho R T, \qquad (2.4)$$

where V_i and x_i represent the velocity and position, respectively. Various thermodynamic properties are represented by ρ (density), p (pressure) and T (temperature), while R and n denotes the gas constant and specific heat ratio, respectively. Equation (2.1) is the continuity equation, equation (2.2) represents the momentum conservation equations, (2.3) is the equation of energy conservation and (2.4) is the equation of state for a perfect gas. Heat flux (q_k) and the viscous stress tensor (σ_{ij}) are found using the following constitutive relationships:

$$\sigma_{ij} = \mu \left(\frac{\partial V_i}{\partial x_j} + \frac{\partial V_j}{\partial x_i} \right) + \delta_{ij} \lambda \frac{\partial V_k}{\partial x_k}; \qquad (2.5)$$

$$q_k = -K \frac{\partial T}{\partial x_k}, \qquad (2.6)$$

where K is the thermal conductivity, μ is the first coefficient of viscosity and λ denotes the second coefficient of viscosity ($\lambda = -(2\mu/3)$).

In this work we use the symbol A_{ij} to denote the components of the velocity-gradient tensor,

$$A_{ij} \equiv \frac{\partial V_i}{\partial x_j}. \qquad (2.7)$$

By taking the gradient of momentum (2.2), the exact evolution equation of A_{ij} can be obtained,

$$\frac{DA_{ij}}{Dt} = -A_{ik}A_{kj} - \underbrace{\frac{\partial}{\partial x_j}\left(\frac{1}{\rho}\frac{\partial p}{\partial x_i} \right)}_{\mathbb{P}_{ij}}$$
$$+ \underbrace{\frac{\partial}{\partial x_j}\left\{ \frac{1}{\rho}\frac{\partial}{\partial x_k}\left[\mu \left(\frac{\partial V_i}{\partial x_k} + \frac{\partial V_k}{\partial x_i} - \frac{2}{3}\frac{\partial V_p}{\partial x_p}\delta_{ik} \right) \right] \right\}}_{\Upsilon_{ij}}, \qquad (2.8)$$

where $\mathbb{P}_{ij}$ is the pressure Hessian tensor and Υ_{ij} is the viscous process governing the evolution of the velocity-gradient tensor. The rate of change following a fluid particle is calculated using the substantial derivative, which is represented by the operator $D/Dt(\equiv (\partial/\partial t) + V_k \partial/\partial x_k)$.

3. Direct numerical simulations and particle tracking

Our direct numerical simulations have been performed using the gas kinetic method (GKM). GKM was originally developed by Xu (2001) and has been shown to be quite robust in terms of numerical stability. Further, GKM has the ability to capture shocks without producing numerical oscillations. In the recent past several researchers have employed GKM to simulate compressible decaying turbulence (Kerimo & Girimaji 2007; Liao, Peng & Luo 2009; Kumar, Girimaji & Kerimo 2013; Parashar *et al.* 2017*b*).

Simulation	M_t	Re_λ	Grid size	A_0	κ_0
A	0.488	175	256^3	0.011	4
B	0.4	250	1024^3	0.00066	4
C	0.6	250	1024^3	0.0015	4
D	0.8	250	1024^3	0.0027	4
E	0.075	70	256^3	0.000023	4

TABLE 1. Initial parameters of DNS simulations.

Our computational domain is of size 2π with a uniform grid and periodic boundary conditions imposed on opposite sides of the domain. The initial velocity field is generated at random with zero mean and having the following energy spectrum $E(\kappa)$:

$$E(\kappa) = A_0 \kappa^4 \exp\left(-2\kappa^2/\kappa_0^2\right), \tag{3.1}$$

where κ is the wavenumber. Values for spectrum constants A_0 and κ_0 are provided in table 1 for various simulations employed in this work. The initial temperature, pressure and density fields are uniform. The relevant Reynolds number for isotropic turbulence is the one based on Taylor micro-scale (Re_λ),

$$Re_\lambda = \sqrt{\frac{20}{3\epsilon\nu}} k, \tag{3.2}$$

where k, ϵ and ν represent turbulent kinetic energy, its dissipation rate and kinematic viscosity. For compressible isotropic turbulence, the relevant Mach number is the turbulent Mach number (M_t),

$$M_t = \sqrt{\frac{2k}{nR\overline{T}}}, \tag{3.3}$$

where $\overline{T}$ represents mean temperature. Following the work of Kumar *et al.* (2013), we have used a fourth-order accurate weighted essentially non-oscillatory (WENO) method for interpolation of flow variables. Various parameters of the simulations are presented in table 1.

We first show validation of the results from our numerical scheme (GKM) against high-order compressible results of Samtaney, Pullin & Kosovic (2001) (Simulation A, table 1). In figure 1(a) we present the evolution of turbulent kinetic energy (k). In figure 1(b), we present the root mean square (r.m.s.) velocity divergence (θ) which is defined as,

$$\theta = \left\langle \left(\frac{\partial V'_i}{\partial x_i}\right)^2 \right\rangle^{1/2}, \tag{3.4}$$

where $'$ denotes fluctuation. Further, in figure 1(c), we plot the probability distribution function of the local Mach number (M_{loc}), where

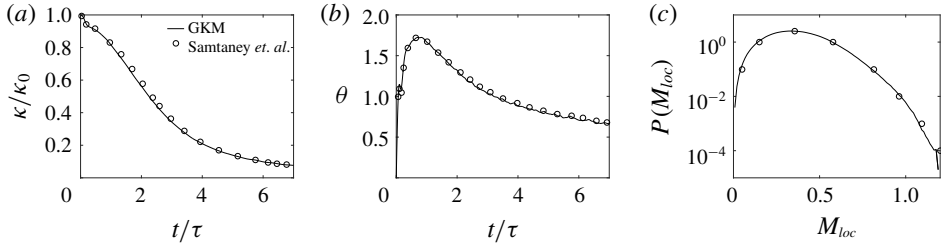$$M_{loc} = \sqrt{\frac{V'_i V'_i}{nRT}}. \tag{3.5}$$

FIGURE 1. Validation of the GKM solver. PDF of M_{loc} is presented at 1.56 eddy-turnover times.
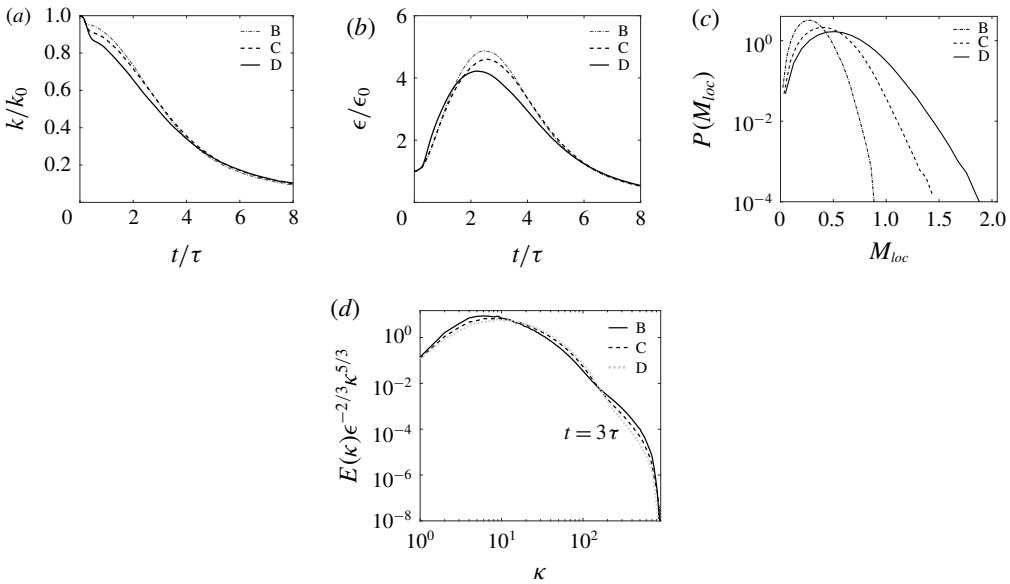

FIGURE 2. Evolution of (*a*) normalised turbulent kinetic energy k/k_0, (*b*) normalised dissipation rate (ϵ/ϵ_0), (*c*) PDF of local Mach number and (*d*) normalised energy spectra of Simulations B–D ($t = 3\tau$).

Note that time in these figures have been normalised using τ, which represents the eddy-turnover time (Yeung & Pope 1989; Elghobashi & Truesdell 1992; Samtaney *et al.* 2001; Martín *et al.* 2006),

$$\tau = \frac{\lambda_0}{u'_0}, \tag{3.6}$$

where u'_0 is the root mean square (r.m.s.) velocity, and λ_0 is the integral length scale of the initial flow field (at time, $t = 0$). It can be observed that for all the three statistics shown in figure 1, the results from GKM show excellent agreement with the results of Samtaney *et al.* (2001). In figures 2(*a*) and 2(*b*) we present the evolution of turbulent kinetic energy (k) and dissipation rate (ϵ) of Simulations B–D. In figures 2(*c*) and 2(*d*) we present the PDF of local Mach number and energy spectra at $t = 3\tau$ of Simulations B–D.

For our study various Lagrangian statistics are obtained using a Lagrangian particle tracker (LPT), which extracts the time history of tagged fluid particles. The trajectory

$(X^+(y, t))$ of a fluid particle is obtained (using LPT) by solving the following equation of motion:

$$\frac{\partial X^+(t, y)}{\partial t} = V(X^+(t, y), t), \tag{3.7}$$

where y indicates the label/tag assigned to the fluid particle at the initial time ($t = 0$) and the superscript '+' represents Lagrangian flow variable (or equivalently, y). To comply with the initial uniform density field, we consistently choose initial values of X^+ at random using the uniformly distributed probability density function of the spatial coordinates at $t = 0$. Subsequently, equation (3.7) is integrated using a second-order Runge–Kutta method. As suggested by Yeung & Pope (1988), we employ a cubic spline based interpolation to find flow properties at spatial locations which do not coincide with the grid points of the computational domain. Further details of validation of our DNS solver and LPT algorithm are available in Danish *et al.* (2016*a*) and Parashar *et al.* (2017*a*). In the next sections, unless specified otherwise, results are presented from Simulation D.

4. Velocity-gradient invariants and flow-field topology

The topology associated with a fluid element is the local streamline pattern in its vicinity as observed with respect to a reference frame which is purely translating with the centre of mass of the fluid element. Topology depends on the nature of the eigenvalues of the local state of the velocity-gradient tensor. However, it can also be inferred with a knowledge of the three invariants (P, Q, R) of the velocity-gradient tensor,

$$\text{and} \quad \begin{rcases} P = -A_{ii}; \quad Q = \tfrac{1}{2}(P^2 - A_{ij}A_{ji}); \\ R = \tfrac{1}{3}(-P^3 + 3PQ - A_{ij}A_{jk}A_{ki}). \end{rcases} \tag{4.1}$$

Correspondingly, the invariants (p, q, r) of the normalised velocity-gradient tensor (a_{ij}) are defined as Suman & Girimaji (2010):

$$\begin{rcases} a_{ij} = \dfrac{A_{ij}}{\sqrt{A_{mn}A_{mn}}}; \quad p = -a_{ii}; \\ q = \tfrac{1}{2}(p^2 - a_{ij}a_{ji}); \quad \text{and} \quad r = \tfrac{1}{3}(-p^3 + 3pq - a_{ij}a_{jk}a_{ki}). \end{rcases} \tag{4.2}$$

Chong *et al.* (1990) categorise topological patterns (table 2) of an incompressible field into unstable-node-saddle-saddle (UNSS), stable-node-saddle-saddle (SNSS), stable-focus-stretching (SFS) and unstable-focus-compressing (UFC). In compressible flows, four additional major topologies can exist: stable-focus-stretching (SFS) and stable-node/stable-node/stable-node (SNSNSN), which are associated with contracting fluid particles, and unstable-focus-stretching (UFS) and unstable-node/unstable-node/unstable-node (UNUNUN), which are associated with expanding fluid particles. Figure 3 shows different regions in the p–q–r space associated with different topologies. The reader is referred to Chong *et al.* (1990) for further details on flow-field topology.

Since the value of the three invariants of the velocity-gradient tensor uniquely determines the topology associated with a local fluid element, the dynamics of topology can be studied in terms of the dynamics of the invariants themselves. Using
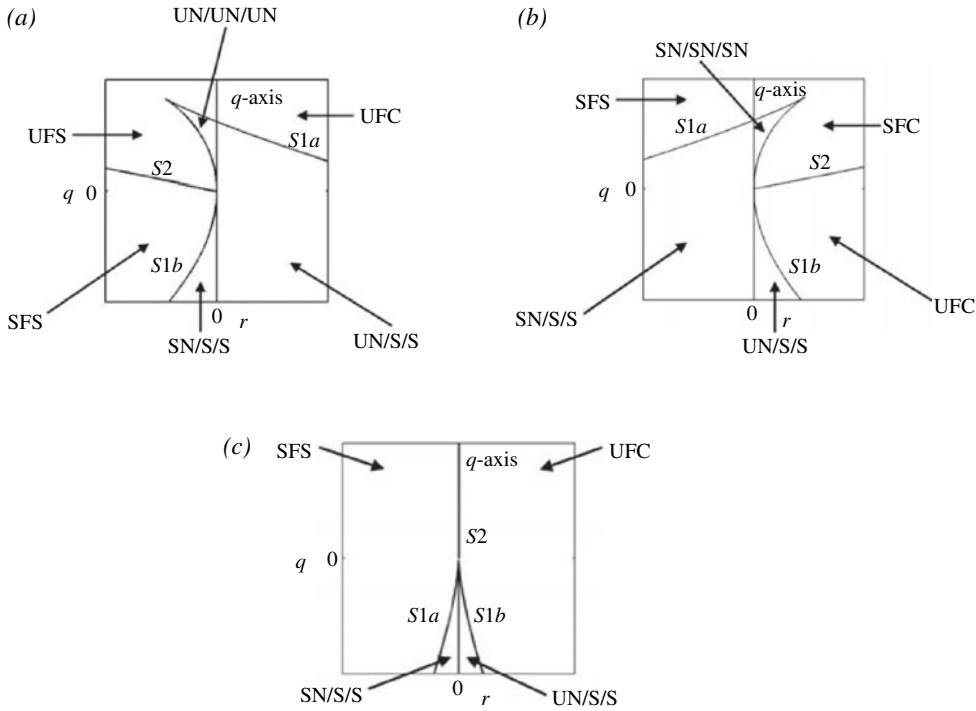
FIGURE 3. Regions of different flow topologies in different p-planes: (a) $p < 0$, (b) $p > 0$ and (c) $p = 0$.

the evolution equation of the velocity-gradient tensor (2.8), the time evolution of invariants (P, Q, R) can be expressed (Bechlars & Sandberg 2017a),

$$\left.\begin{aligned}
\frac{\mathrm{d}P}{\mathrm{d}t} &= P^2 - 2Q - S_{ii}; \\
\frac{\mathrm{d}Q}{\mathrm{d}t} &= QP - \frac{2P}{3}S_{ii} - 3R - A_{ij}S_{ji}^*; \\
\frac{\mathrm{d}R}{\mathrm{d}t} &= -\frac{Q}{3}S_{ii} + PR - PA_{ij}S_{ji}^* - A_{ik}A_{kj}S_{ji}^*,
\end{aligned}\right\} \quad (4.3)$$

where S_{ij} is the source term in the evolution equation of velocity-gradient tensor (2.8) and the symbol S_{ij}^* is the traceless part of the S_{ij} tensor,

$$\left.\begin{aligned}
S_{ij} &= -\mathbb{P}_{ij} + \Upsilon_{ij}; \\
S_{ij}^* &= S_{ij} - \frac{S_{kk}}{3}\delta_{ij}.
\end{aligned}\right\} \quad (4.4)$$

Here $\mathbb{P}_{ij}$ is the pressure Hessian tensor and Υ_{ij} represents the viscous process in the evolution equation of the velocity-gradient tensor (2.8).

The relationship between the non-normalised invariants (P, Q, R) and normalised invariants (p, q, r) is

$$p = \frac{P}{\sqrt{A_{ij}A_{ij}}}; \quad q = \frac{Q}{A_{ij}A_{ij}}; \quad \text{and} \quad r = \frac{R}{(A_{ij}A_{ij})^{3/2}}. \quad (4.5a\text{--}c)$$

Acronyms	$p = 0$	$p < 0$	$p > 0$	Eigenvalues of a_{ij}
SFS	$r < 0$	$r < 0$ and $S2 > 0$	$r < 0$	Complex
UFC	$r > 0$	$r > 0$	$r > 0$ and $S2 < 0$	Complex
UNSS	$r > 0$ and $q < 0$	$r > 0$	$r > 0$ and $q < 0$	Real
SNSS	$r < 0$ and $q < 0$	$r < 0$ and $q < 0$	$r < 0$	Real
UFS	—	$r < 0$ and $S2 < 0$	—	Complex
UN/UN/UN	—	$r < 0$ and $q > 0$	—	Real
SFC	—	—	$r > 0$ and $S2 > 0$	Complex
SN/SN/SN	—	—	$q > 0$ and $r > 0$	Real

TABLE 2. Zones of various topologies in p–q–r space, where acronyms are: stable-focus-stretching (SFS), unstable-focus-compressing (UFC), unstable-node/saddle/saddle (UNSS), stable-node/saddle/saddle (SNSS), unstable-focus-stretching (UFS), unstable-node/unstable-node/unstable node (UN/UN/UN), stable-focus-compressing (SFC), stable-node/stable-node/stable-node (SN/SN/SN). S1 and S2 are the curves separating the regions of real and imaginary eigenvalues of A (Chong *et al.* 1990).

Using (4.3) and (4.5a–c), the evolution equation of the normalised invariants (p, q, r) can be derived as:

$$\left.\begin{aligned}
\frac{dp}{dt} &= \frac{d}{dt}\left(\frac{P}{\sqrt{A_{ij}A_{ij}}}\right) = \frac{1}{\sqrt{A_{ij}A_{ij}}}\frac{dP}{dt} - \frac{P}{(A_{ij}A_{ij})^{3/2}}A_{ij}\frac{dA_{ij}}{dt}; \\
\frac{dq}{dt} &= \frac{d}{dt}\left(\frac{Q}{A_{ij}A_{ij}}\right) = \frac{1}{A_{ij}A_{ij}}\frac{dQ}{dt} - \frac{2Q}{(A_{ij}A_{ij})^2}A_{ij}\frac{dA_{ij}}{dt}; \\
\frac{dr}{dt} &= \frac{d}{dt}\left(\frac{R}{(A_{ij}A_{ij})^{3/2}}\right) = \frac{1}{(A_{ij}A_{ij})^{3/2}}\frac{dQ}{dt} - \frac{3R}{(A_{ij}A_{ij})^{5/2}}A_{ij}\frac{dA_{ij}}{dt}.
\end{aligned}\right\} \quad (4.6)$$

While following an identified fluid particle in physical space and tracking its invariants information, we can track the footprints of the fluid particle in the p–q–r space as well. We refer to such a trajectory of the fluid particle in p–q–r space as the Lagrangian trajectory (LT).

5. Lifetimes of topologies

Two pertinent questions to address while studying the dynamics of velocity gradients and flow-field topology are how long a topology lasts, and how compressibility influences that. In this section we address these questions. We quantify the lifetime of a topology as the time it takes for a fluid particle to change its topology from the one it had at a reference time t_{ref}. We express this time non-dimensionalised by the Kolmogorov time scale (τ_κ) of the homogeneous flow field at t_{ref}. We refer to the normalised lifetime of a given topology ($\mathcal{T}$) thus obtained as

$$L_\mathcal{T} = 2\frac{t^* - t_{ref}}{\tau_\kappa}, \quad (5.1)$$

where t^* denotes the time instant when the topology $\mathcal{T}$ associated with a tagged fluid particle at t_{ref} changes to some other topology. Correspondingly, the mean value of $L_\mathcal{T}$ is calculated by following a large number of tagged particles which have the same topology $\mathcal{T}$ at t_{ref},

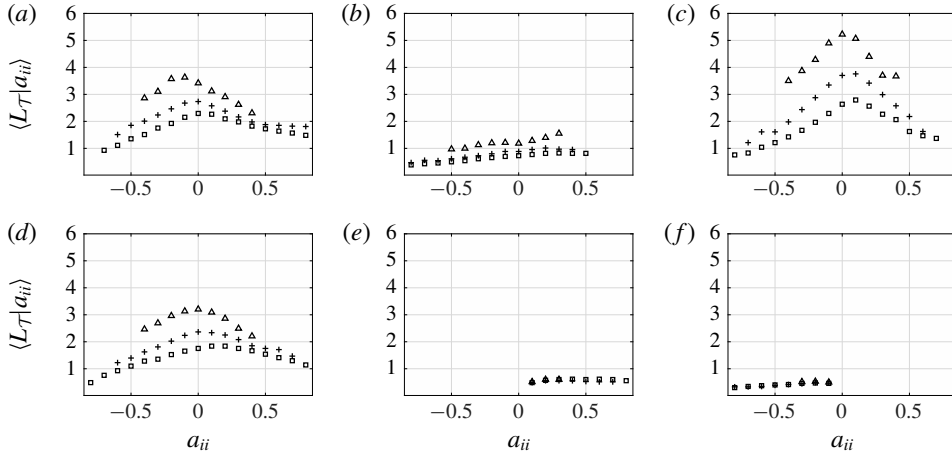$$\langle L_\mathcal{T}\rangle = 2\frac{\langle t^* - t_{ref}\rangle}{\tau_\kappa}, \quad (5.2)$$

FIGURE 4. Value of $\langle L_T|a_{ii}\rangle$ (bin size $a_{ii}\pm0.05$) for 6 major topologies: (*a*) UNSS, (*b*) SNSS, (*c*) SFS, (*d*) UFC, (*e*) UFS and (*f*) SFC. Symbol $\triangle$, $+$, $\square$ represent lifetime of topology for Simulations B, C and D, respectively. Here $t_{ref}=3\tau$.

Simulation	UNSS	SNSS	SFS	UFC	UFS	SFC
B	3.35	1.09	5.04	3.13	0.51	0.46
C	2.53	0.83	3.42	2.21	0.50	0.44
D	2.08	0.64	2.37	1.67	0.51	0.43

TABLE 3. Influence of M_t on mean $\langle L_T\rangle$. Flow fields at $t=3\tau$ from Simulations B, C and D have been used.

where $\langle\ \rangle$ represents an averaged value over various LTs. Note that the factor 2 is included in our definitions (5.1) and (5.2) to statistically account for the fact that the particles which are identified with a given topology (T) at a chosen reference time (t_{ref}) for our analysis might not have necessarily attained that topology exactly at t_{ref}; those particles might have existed with that same topological state for some duration prior to t_{ref}.

In our calculations and analysis of lifetime of topologies we employ the data fields of Simulations B–D, and in each case $t_{ref}=3\tau$. A total sample size of $1\,000\,000$ particles is used for calculating the mean lifetime of the topologies. To identify the role of compressibility on the lifetimes, we examine $\langle L_T\rangle$ conditioned upon discrete values of a_{ii} at the reference time (t_{ref}). These conditioned lifetimes are represented as $\langle L_T|a_{ii}\rangle$.

In table 3 we present mean lifetimes $\langle L_T\rangle$ of topologies. The six major topologies that exist in compressible turbulence are considered (UNSS, SNSS, SFC, SFS, UFC and UFS). We also present mean lifetimes of various topologies conditioned upon different initial dilatation levels ($\langle L_T|a_{ii}\rangle$) in figure 4. Each panel corresponds to a specific topology. Further, to identify the role of initial turbulent Mach number M_t, we have calculated both $\langle L_T\rangle$ and $\langle L_T|a_{ii}\rangle$ using Simulations B–D. All these simulations have identical initial Reynolds number (250), but different initial Mach number (0.4, 0.6 and 0.8).

We observe that the compressibility parameters, dilatation and initial Mach numbers influence the lifetimes of the topologies, but selectively. Mean lifetimes of UNSS (figure 4*a*), UFC (figure 4*c*) and SFS (figure 4*d*) topologies seem to be more sensitive to both the Mach number and dilatation as compared to those of the other topologies. As the level of dilatation increases from high negative values to zero dilatation, lifetimes of these topologies increase. On the other hand, however, as we move from zero to positive dilatation, lifetimes seem to decrease again. Further, the lifetime of these topologies (UNSS, UFC and SFS) tend to decrease with an increase in initial turbulent Mach number as shown in figure 4(*a*,*c*,*d*). In contrast to the UNSS, UFC and SFS topologies, the other three major topologies exiting in a compressible flow field, SNSS, UFS and SFC, seem to last for more or less the same amount of time, showing not much sensitivity to either dilatation rate or Mach number. Further, we would like to mention that the statistics of the lifetimes presented in figure 4 have been found to be fairly independent of the choice of t_{ref} over a wide range, $t_{ref} \in [\tau, 5\tau]$.

5.1. *Factors influencing lifetimes of topologies*

To further understand the behaviour observed in figure 4, we investigate two prospective reasons which may influence the lifetime of a topology of a fluid particle as it moves in the *p–q–r* space: (i) the actual volume available to a topology in the *p–q–r* space, and (ii) the velocity of the fluid particles in the *p–q–r* space. The velocity of a particle in the *p–q–r* space can be defined as the rate at which its three invariants, *p*, *q* and *r*, change with time. This rate is quantified as a velocity vector in the *p–q–r* space. We denote this velocity vector by $\boldsymbol{U}_{pqr}$,

$$\boldsymbol{U}_{pqr} = \frac{\mathrm{d}p}{\mathrm{d}t}\hat{p} + \frac{\mathrm{d}q}{\mathrm{d}t}\hat{q} + \frac{\mathrm{d}r}{\mathrm{d}t}\hat{r}, \quad (5.3)$$

where d*p*/d*t*, d*q*/d*t* and d*r*/d*t* are rates of change of the invariants following a fluid particle in accordance with (4.6). The symbols $\hat{p}$, $\hat{q}$ and $\hat{r}$ denote the unit vectors along the three mutually perpendicular axes of the *p*, *q* and *r* coordinates. The quantity $\boldsymbol{U}_{pqr}$ is indeed a measure of how fast the footprint of a fluid particle is changing in the *p–q–r* space. The component d*p*/d*t*$\hat{p}$ is the rate of movement of a particle perpendicular to the *q–r* plane, whereas d*q*/d*t*$\hat{q}$ + d*r*/d*t*$\hat{r}$ is the projection of $\boldsymbol{U}_{pqr}$ on the *q–r* plane. We denote this part of the velocity vector by $\boldsymbol{U}_{qr}$,

$$\boldsymbol{U}_{qr} = \frac{\mathrm{d}q}{\mathrm{d}t}\hat{q} + \frac{\mathrm{d}r}{\mathrm{d}t}\hat{r}. \quad (5.4)$$

The quantity d*p*/d*t* represents how fast dilatation changes along the trajectories. This is indeed negative of the rate of change in dilatation rate, and thus directly influences fluid density. In numerical simulations of strictly incompressible turbulence, wherein the pressure evolves through Poisson's equation, d*p*/d*t* is trivially zero. However, in compressible flows, the dynamics of the first invariant (*P*) of the velocity-gradient tensor is governed by the imbalance between the pressure and inertial processes. Sarkar, Erlebacher & Hussaini (1991) showed that the r.m.s. of dilatation ($P = p\sqrt{A_{mn}A_{mn}}$) is proportional to the square of the turbulent Mach number in decaying compressible turbulence.

It is expected that a smaller volume available to a topology in the *p–q–r* space will be a contributing factor towards decreasing the lifetime of a topology, because
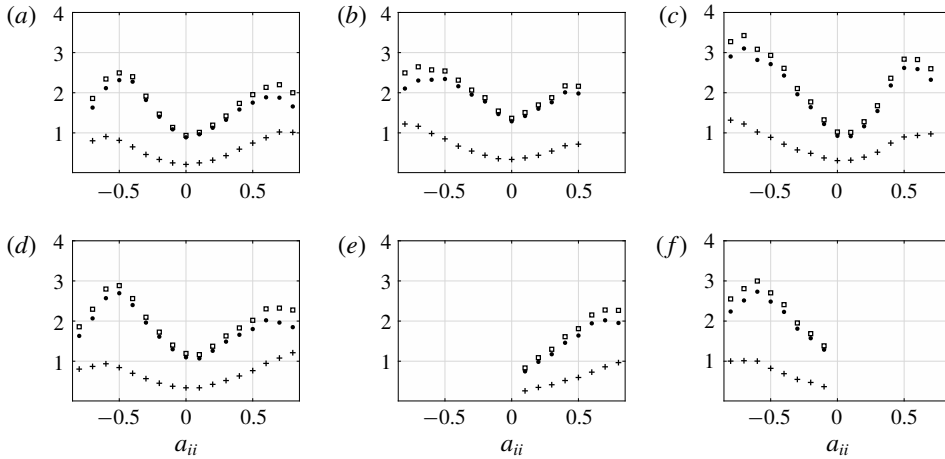
FIGURE 5. Value of $\langle|\boldsymbol{U}_{pqr}|\rangle$ conditioned upon topology ($\mathcal{T}$) and dilatation level (a_{ii}) at $t = 3\tau$ (symbol $\square$), $\langle|\mathrm{d}p/\mathrm{d}t|\rangle$ (symbol $\bullet$) and $\langle|\boldsymbol{U}_{qr}|\rangle$ (symbol $+$) (*a*) UNSS, (*b*) SNSS, (*c*) SFS, (*d*) UFC, (*e*) UFS and (*f*) SFC. (All results from Simulation D.)

p ($-a_{ii}$)	UNSS	SNSS	SFS	UFC	UFS	SFC	SNSNSN	UNUNUN
$-$ve	0.04	0.01	0.08	0.10	0.08	0	0	0.01
$+$ve	0.01	0.04	0.01	0.08	0	0.08	0.01	0

TABLE 4. Available volumes for different topologies in the p–q–r space.

a particle even if moving slowly is expected to cross-over to the territory of a neighbouring topology sooner. On the other hand, a high magnitude of $\boldsymbol{U}_{pqr}$ of a fluid particle in the p–q–r space is expected to bring the particle closer to the bounding surfaces (figure 3) quickly and thus contributing to a reduction in lifetime of the topology associated with that fluid particle. In table 4 we present the volumes associated with the six major topologies that exist in compressible turbulence in the space of the normalised invariants p, q and r. These volumes have been reported separately on the positive and the negative side of the p-axis. In figure 5(*a*–*f*) we present the mean value of $|\boldsymbol{U}_{pqr}|$ calculated by taking the average of $|\boldsymbol{U}_{pqr}|$ conditioned upon topology ($\mathcal{T}$) and dilatation level (a_{ii}) at $t = 3\tau$. Further, conditional means of $|\mathrm{d}p/\mathrm{d}t|$ and $|\boldsymbol{U}_{qr}|$ are also shown.

We observe that in all topologies the trends in the variation of $|\mathrm{d}p/\mathrm{d}t|$ and $|\boldsymbol{U}_{qr}|$ with dilatation (a_{ii}) are qualitatively similar. However, the mean value of $|\mathrm{d}p/\mathrm{d}t|$ seems to be significantly higher than those of $|\boldsymbol{U}_{qr}|$. This observation may give an initial impression that the transition of particles from their original topological states to other states must be driven by the movement of particles along the p-axis alone rather than any significant movement along $\hat{q}$ or $\hat{r}$. However, our investigation shows that despite $|\mathrm{d}p/\mathrm{d}t|$ being the dominant contributor to the magnitude of $\boldsymbol{U}_{pqr}$, the particle-averaged displacement achieved during the elapsed time $t^* - t_{ref}$ in the p-direction is actually comparable to the displacements in the q- and the r-directions (table 5) during the same time period. Thus, topological transitions are not determined by the movement of particles in the p-direction alone: $|\boldsymbol{U}_{qr}|$ is still an important contributor in determining topological transitions and thus the lifetimes of topologies.

a_{ii} at t_{ref}	Along $\hat{p}$	Along $\hat{q}$	Along $\hat{r}$
-0.5	0.11	0.09	0.10
0	0.05	0.09	0.08
$+0.5$	0.12	0.11	0.12

TABLE 5. Particle-averaged magnitudes of net displacements along the $\hat{p}$, $\hat{q}$ and $\hat{r}$ directions during $t^* - t_{ref}$ (5.1) (normalised by $2\sqrt{3}$, 1 and $2\sqrt{3}/9$, respectively; these numbers are the algebraic extents of p, q and r, respectively).

We now examine if the volume measures available in table 4 and the conditional mean values of $|U_{pqr}|$ available in figure 5 can help us understand the variation of the lifetimes reported in figure 4. We begin our discussion with the UNSS and SNSS topologies. In figure 5 we observe that the mean value of $|U_{pqr}|$ is higher at positive/negative dilatations than what it is at zero dilatation. Moreover, if we compare only the high positive and high negative dilatations, the mean velocity is somewhat higher at negative dilatations. On the other hand, table 4 shows that the available volume of the UNSS topology on the negative side is less than what it is on the positive side. A higher mean velocity associated with a smaller volume on the $a_{ii} < 0$ side allows a particle with initial UNSS topology to quickly cross-over to the territory of the neighbouring topologies, making its lifetime low, as observed in figure 4(*a*). At zero dilatation, the velocity drops significantly, thus allowing the fluid element to stay inside the UNSS territory for a longer duration. At positive dilatation levels, even though the velocity is high, a significant increase in the volume of UNSS allows the lifetime to decrease moderately, as evident in figure 4(*a*). In the case of the SNSS topology, as dilatation increases from high negative dilatation to high positive dilatation levels, the volume decreases. Velocity, however, decreases from a high value at negative to a very low value at zero dilatation (figure 5*b*). The drop in the available volume seems to be offset by a decrease in velocity keeping the average lifetime of the topology more or less at the same level as it was at high negative dilatation. When dilatation increases to positive values, velocity increases (figure 5) – although not as much as it was at the negative dilatations and thus, even a decrease in volume results in only a small increase in the lifetime (figure 4*b*). A similar explanation can be provided for the variation in lifetimes observed in figures 4(*c*) and 4(*d*) for the SFS and UFC topologies using the volume data and the mean magnitude of $|U_{pqr}|$ of these topologies in figures 5(*c*) and 5(*d*).

For the UFS and SFC topologies, we do not observe any change in lifetimes in figure 4(*e*). While UFS exists only at positive dilatation, SFC exists only at negative dilatations. For both these topologies, the volumes increase as the magnitude of the dilatation increases (table 4). Further, figure 5(*e*) clearly shows that their velocities also increase as the magnitude of the normalised dilatation increases. For both these topologies, the increase in volume (which favours high lifetime) seem to be effectively counteracted by an increase in mean velocity (which favours low lifetime) resulting in an almost dilatation-independent lifetime, as evident in figure 4.

5.1.1. *Role of Mach number*

In general, the influence of increasing initial turbulent Mach number is to decrease the lifetime of the topologies (figure 4). The explanation for this trend is provided by table 6, wherein we have included the mean magnitude of U_{pqr} in Simulations B–D at

Simulation	UNSS	SNSS	SFS	UFC	UFS	SFC
B	0.85	1.15	0.79	0.97	1.30	1.98
C	1.04	1.54	1.11	1.25	1.35	2.10
D	1.31	1.97	1.45	1.53	1.36	2.14

TABLE 6. Influence of M_t on mean of $|U_{pqr}|$. Flow field at $t = 3\tau$ from Simulation D has been used.

UNSS	SNSS	SFS	UFC	UFS	SFC
28.17	9.95	31.00	21.25	5.81	3.82

TABLE 7. Percentage topology composition in Simulation D.

$t = 3\tau$. We observe that, in general, an increase in the initial turbulent Mach number increases mean value of $|U_{pqr}|$, consequently reducing $\langle L_{\mathcal{T}} \rangle$ as evident in figure 4. It is plausible to attribute this observed enhancement in the magnitude of $\bar{U}_{pqr}$ to the increased importance of the inertial processes as compared to the pressure-related processes in the evolution equations of the invariants (4.6) as Mach number increases. To ascertain the veracity of this conjecture, however, a much more detailed analysis of the various tensorial interactions between the velocity gradient and the pressure Hessian tensors incumbent in (4.6) is required. The authors deem such an analysis to be too involved for it to be adequately addressed within the scope of the present study.

Overall, our results in table 3 clearly show that, in terms of longevity, the six major topologies existing in compressible turbulence can be arranged in the following descending order: SFS>UNSS>UFC>SNSS>UFS>SFC. Accordingly, it is plausible to expect that at a typical instant of this simulation, compressible decaying turbulence should have the highest population of particles associated with the SFS topology, the lowest with the SFC topology and populations of the other four topologies falling in the same order as the order of their lifetimes. In table 7 we present the population percentage of each of the six topologies at $t = 3\tau$ in Simulation D. This percentage composition has been computed by averaging over Lagrangian trajectories. Since initial seeding of Lagrangian trajectories has been done at $t = 0$ when the density is uniform in the flow domain, this Lagrangian based averaging is equivalent to mass-weighted averaging. We observe that indeed the percentage populations of the six topologies decrease exactly in the same order as the order shown by them in terms of lifetimes.

5.2. *Conversion tendencies of topologies*

In the previous section we quantified the lifetimes of different topologies and examined the influence of compressibility on them. Besides these estimates of lifetimes, it is also pertinent to investigate the relative inclinations of a given topology to convert into other possible topological structures in a compressible flow field. In figure 6 we show time evolution of the percentage topology composition of a sample initially composed of 100 % of a chosen topology ($\mathcal{T}$). For example, in figure 6(*a*) we show the evolution of the percentage topology composition of a sample initially composed of 100 % UNSS topology (calculated by averaging over LTs). It can be observed in figure 6(*a*) that within approximately one eddy-turnover time the 100 %
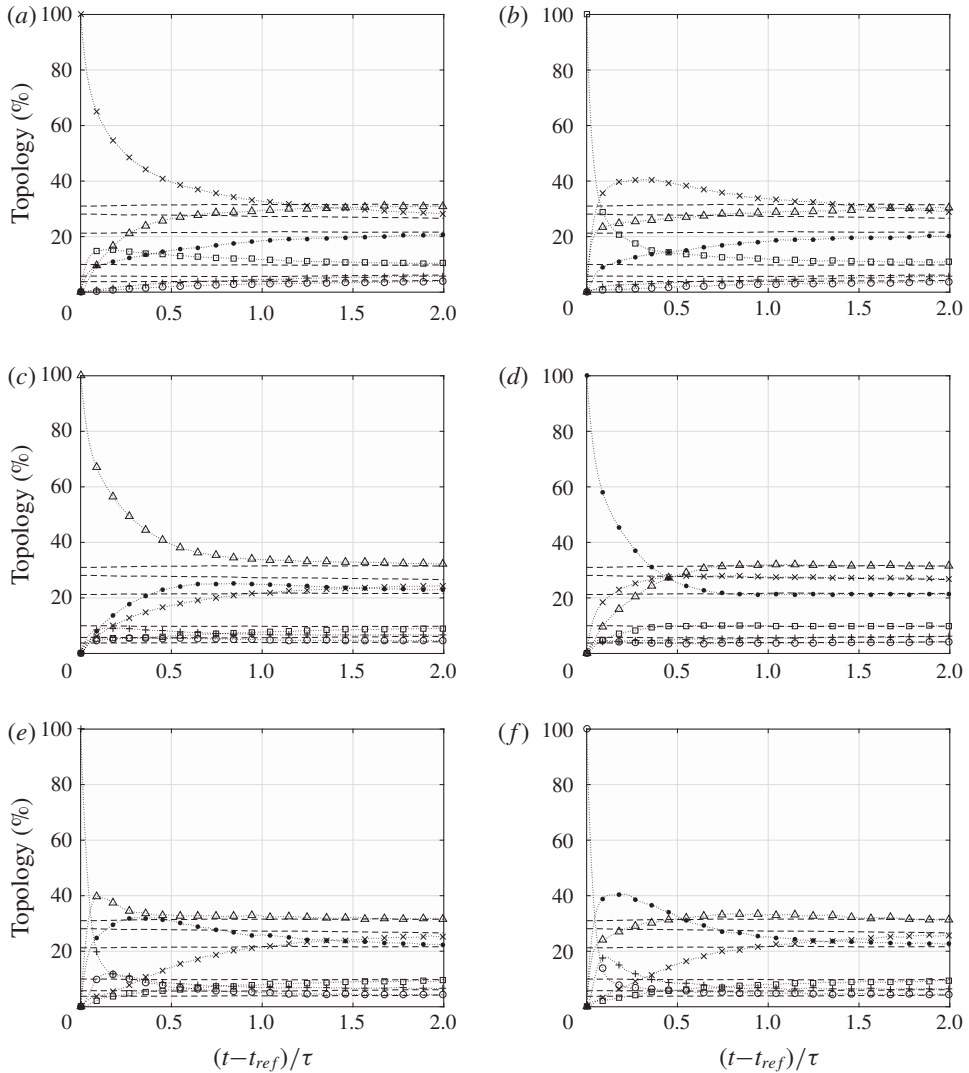
FIGURE 6. Evolution of percentage composition of topology starting from 100 % (*a*) UNSS, (*b*) SNSS, (*c*) SFS, (*d*) UFC, (*e*) UFS and (*f*) SFC topology (Simulation D, $t_{ref} = 3\tau$). Different symbols represent six major topologies: $\times$ (UNSS), $\square$ (SNSS), $\triangle$ (SFS), $\bullet$ (UFC), $+$ (UFS) and $\circ$ (SFC). Dashed lines represent the global composition of a topology, which is also presented as a percentage in table 7 and is found to be almost invariant with time.

UNSS sample spreads throughout the $p - q - r$ space in a proportion that mimics the global topology composition (table 7). Similar trends are observed for other topologies as well (shown in figure 6*b–f*).

Figure 6 is useful for demonstrating the asymptotic tendency of a sample comprising of a given topology to transform and spread to other possible topologies and eventually merge with the composition of the unconditioned sample. However, it does not explicitly demonstrate what the most preferred transformation paths (or the
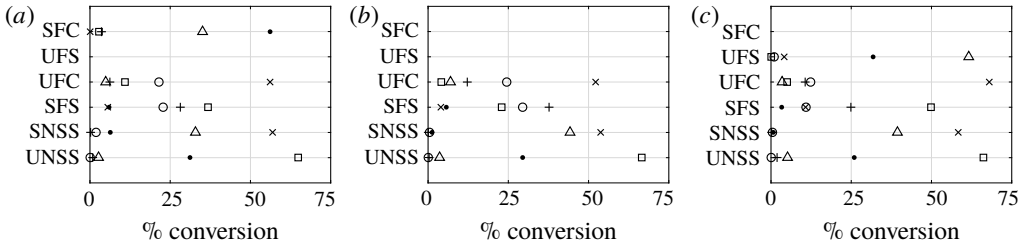
FIGURE 7. Conversion tendencies of various topologies at t^* (5.1) in compressible turbulence. At t_{ref} each sample of particles has 100% of a given topology. Different symbols represent: $\times$ (UNSS), $\square$ (SNSS), $\triangle$ (SFS), $\bullet$ (UFC), $+$ (UFS) and $\circ$ (SFC). (*a*) $a_{ii} = -0.5$, (*b*) $a_{ii} = 0$ and (*c*) $a_{ii} = 0.5$.

dominant conversion tendencies) of a chosen topology are and how these tendencies may be influenced by the initial dilatation level of a fluid particle.

In figure 7 we present the conversion tendencies of particles having three representative dilatation levels at t_{ref}: $a_{ii} = -0.5$, $a_{ii} = 0$ and $a_{ii} = 0.5$ (figures 7*a*, 7*b* and 7*c*, respectively). In each of these figures, the *y*-axis represents a sample of particles with 100% population of a given topology. On the *x*-axis we show the percentage of various other topologies which are generated when the particles of the original sample undergo their first transformation (at t^*). For example, the first horizontal level in figure 7(*a*) shows that a sample comprising of 100% UNSS topology eventually breaks down predominantly into SNSS (approximately 70%) with the remainder being the UFC topology (approximately 30%). Similarly, other horizontal levels can be followed to arrive at the conversion percentages starting with other topological states and dilatation levels. To help the reader to visualise the major conversion tendencies that exist in compressible turbulence, in figure 8 we present a qualitative picture of the dominant conversion tendencies of various topologies. Arrows are based only on those conversions which are more than 20% of the original sample (see figure 7). Note that these arrows represent major conversion tendencies and not necessarily the trajectories themselves. The corresponding transitions may involve significant displacements along the *p*-axis as well. A similar analysis on topology conversion can also be performed for incompressible flows. In figure 9, we present the conversion tendency of particles in a nearly incompressible flow field (Simulation E). It can be observed that, for all the topologies, there is a significant conversion tendency in both the clockwise and anticlockwise directions.

5.3. *CMT versus LT*

As mentioned in the Introduction, many researchers have adopted an alternate, although approximate, procedure of examining the topology dynamics in the *p–q–r* space. This alternative method does not track the individual fluid particles at different time instants, but uses the averaged value of the right-hand side of (4.6) conditioned on a chosen set of *p*, *q* and *r* merely at one single time instant. The statistics thus obtained are essentially the conditional averages of the rate of change of the invariants with the conditional parameters being the local values of *p*, *q* and *r*. The trajectories thus obtained are presented as the instantaneous streamlines in *p–q–r* space. Such trajectories are referred to as the conditional mean trajectories (CMT) (Martín *et al.* 1998). CMTs are approximate, and their use in past studies can only be justified as
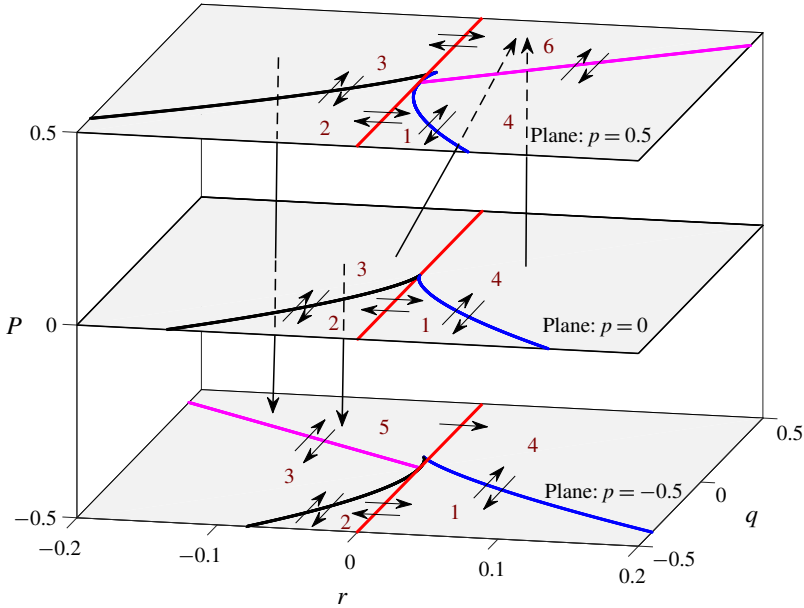
FIGURE 8. (Colour online) An illustration depicting major tendencies of topological transitions in compressible isotropic turbulence. Note that the arrows indicate major conversion tendencies and not necessarily the trajectories themselves. Three representative q–r planes are shown at $a_{ii} = -0.5$, $a_{ii} = 0$ and $a_{ii} = 0.5$. Numbers represent: 1-UNSS, 2-SNSS, 3-SFS, 4-UFC, 5-UFS and 6-SFC.
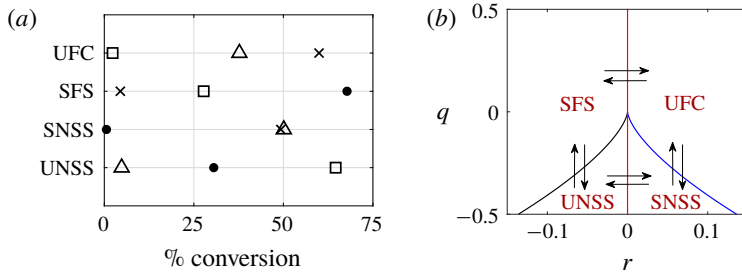

FIGURE 9. (Colour online) (*a*) Conversion tendencies of various topologies at t^* in incompressible turbulence (details of the symbols are given in the caption of figure 7). (*b*) Pictorial representation of major tendencies of topological transitions in incompressible isotropic turbulence.

a surrogate tool in the absence of adequate computational resources (Martín *et al.* 1998).

To further underline the significance of our present work using Lagrangian trajectories, we present table 8, wherein we have included mean values of the lifetimes of the UNSS, SNSS, SFS and UFC topologies computed using the flow fields of Simulation E. Note that Simulation E has a very low initial Mach number and can be treated practically as an incompressible flow. The percentage composition in terms of the four topologies in this flow field is included in table 8. Note that

	UNSS	SNSS	SFS	UFC
% Composition	27.2	7.6	38.5	26.6
Lifetime $\langle L_\mathcal{T} \rangle$	3.60	1.06	6.64	4.16
% Time (LTs)	26.9	7.4	39.2	26.4
% Time (CMTs HIT, Martín *et al.* (1998))	53	5.5	21.5	20.0
% Time (CMTs TBL, Elsinga & Marusic (2010))	15	8	39	38

TABLE 8. Comparison of the performances of CMTs versus the approach adopted in this work. The data in the first three rows are from Simulation E of this work. (HIT, homogeneous isotropic turbulence, TBL, turbulent boundary layer).

the topology composition in this case has also been computed using averages across Lagrangian trajectories. However, since this is a nearly incompressible flow, the density does not change significantly. Thus the averages over Lagrangian trajectories are almost the same as volume-based averaging.

We observe that the mean lifetimes calculated using our Lagrangian approach for these four topologies are in almost the same proportion as the percentage population of the topologies. Further, we present the time spent by the particles in different topologies during a time interval of three eddy-turnover times, calculated using LTs (third row of table 8). We find that, like $L_\mathcal{T}$, the percentage of time spent by the particles in different topologies is also almost similar to the percentage composition of topology. In the last row of table 8 we have included the percentage of 'time spent in various topologies' as calculated by Martín *et al.* (1998) using their CMT approach. Since Martín *et al.*'s (1998) CMTs do show a cyclic change in topology (UFC → UNSS → SNSS → SFS → UFC), the 'time spent in various topologies' can be interpreted as the 'CMT-based estimate of lifetime of topologies'. We find that the proportion of lifetimes calculated using CMTs are in gross disagreement with the percentage composition of topology in incompressible turbulence. In table 8 we have included the CMT-based calculations from the DNS of turbulent boundary layers (Elsinga & Marusic 2010) as well. Even though the proportions of the elapsed duration in various topologies predicted by the CMT-based calculations in the boundary layer are not as skewed as observed in the CMT-based calculations of isotropic turbulence of Martín *et al.* (1998), these proportions still do not show as good an agreement as shown by the LT-based calculations.

To elucidate why CMTs fail in capturing topology lifetimes (and probably other time-dependent aspects of the dynamics of velocity gradients), we present a simple comparison. In figure 10(*a*) we show a conditional mean trajectory (solid line) originating at point ($q = 0.3$, $r = -0.05$). This CMT has been generated using a one-time Eulerian field from incompressible Simulation E. The CMT shows a spiralling path around the origin. Performing a procedure of line integrations along such trajectories, Martín *et al.* (1998) estimate the characteristic 'cycle time' of topology interconversion as three eddy-turnover times. Next, we tag the same particles (in total 5000) which were having their initial invariants in the vicinity of ($q = 0.3$, $r = -0.05$) at the reference time of four eddy-turnover times and track their movement on the q–r plane. The locations of these 5000 particles after just one eddy-turnover time is shown in figure 10(*a*). It can be observed that the tagged population of particles spreads vastly over the q–r plane. Indeed the spread of this population sample is identical to the characteristic global distribution of particles in the entire flow field. This characteristic distribution has a teardrop shape with the
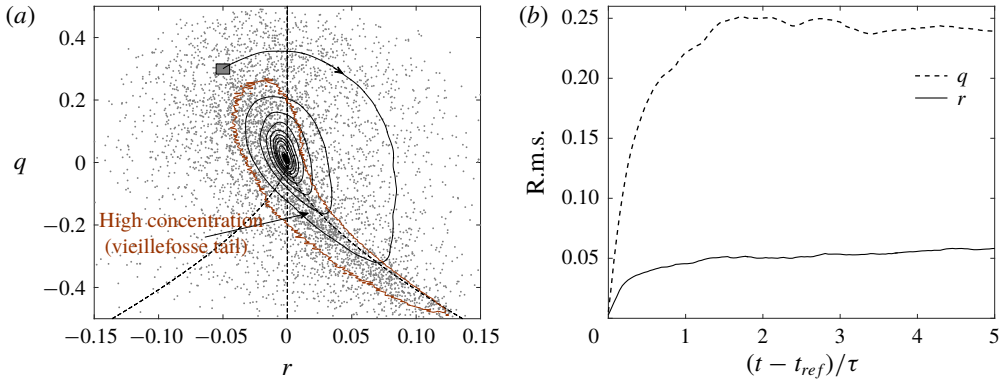
FIGURE 10. (Colour online) (*a*) Instantaneous CMT (solid line) and final spread of
particles (grey dots) after one eddy-turnover time starting from r (-0.05 ± 0.01) and q
(0.3 ± 0.025). (*b*) Evolution of root mean squared value of invariants q and r starting
from r (-0.05 ± 0.01) and q (0.3 ± 0.025).

bulk of data concentrated on one side in the SFC region and on the other side along
the curve separating the UFC and UNSS regions (the so-called Vieillefosse curve,
Vieillefosse (1982), Ashurst *et al.* (1987*b*)).

Further, in figure 10(*b*), we present the root mean squared (r.m.s.) values of q and
r of the same sample of 5000 particles which had their q, r in the vicinity of ($q =
0.3$, $r = -0.05$) at the reference time of four eddy-turnover times. The r.m.s. values
start increasing and within just one eddy-turnover time reach their asymptotic states:
the r.m.s. of q reaches an asymptotic state of 0.24, and the r.m.s. of r reaches an
asymptotic state of 0.05. Indeed, these values match with the unconditioned r.m.s.
values of q and r of all the particles that are present in the flow field. Thus, even one
eddy-turnover time is a long enough duration for particles to completely forget their
initial association with a particular point in the q–r plane. Thus, employing CMTs to
estimate phenomena which happen over such time scales is indeed not appropriate.

6. Significance and implications of this work

(i) The question of how long the fluid particles of a turbulent flow field reside in
vortical regions compared to strain-dominated regions is of fundamental interest.
Examples of the context of this question can be found in geophysical flows. The
residence time of a fluid particle in a vortical region is expected to enhance
its acceleration, which in turn has consequences for the formation of raindrops
(Pinsky & Khain 1997; Falkovich, Fouxon & Stepanov 2002; Biferale & Toschi
2005; Toschi *et al.* 2005). The same question finds pertinence in the context
of astrophysics as well (Armitage 2010; Pater & Lissauer 2015). To further
highlight the significance of this question, Bhatnagar *et al.* (2016) goes to the
extent of relating the time spent by a typical fluid particle in a vortical region
to the lifetime of vortices themselves that exist in the flow field. In line with
the motivation to answer this fundamental question, the present paper provides
a detailed Lagrangian investigation and the corresponding estimates of times
spent by fluid particles in various topologies existing in a compressible flow
field. Each of these topologies represents specific patterns of streamlines and is
representative of the relative importance of the rotation rate, strain-rate tensor and

the dilation rate in the flow field. Indeed our results show that even within the broad classification of so-called vortical (or focal) topologies, there are significant differences in lifetimes (see figure 4) associated with SFC, SFS UFS and UFC, all of which are focal topologies. Further, we would like to emphasise that our study examines the influence of compressibility as well on these statistics, and is thus relevant for high Mach number flows as well.

(ii) The velocity gradient is a key quantity in the closure of Lagrangian probability density function (PDF) methods (Pope 2000). Computing velocity gradients, in turn, requires modelling of several incumbent unclosed terms like the pressure Hessian and the viscous processes (Cantwell 1992). While in incompressible flows, a well-accepted model for these processes has already been in place (the recent fluid deformation closure model or the RFDM of Chevillard *et al.* (2008)), the quest for an equally reliable model in compressible flows continues. Recent DNS-based studies of compressible turbulence have shown that several aspects of the local velocity-gradient tensor are strongly influenced by the local instantaneous topological state and dilatation (Danish *et al.* 2016*a*,*b*; Parashar *et al.* 2017*a*). Thus, it seems viable to attempt to model the unclosed terms of the dynamics of velocity gradients conditioned upon local dilatation and topology rather than attempt to develop unconditioned models in the traditional way. Indeed, some attempts in this direction have already been made for modelling velocity-gradient–scalar-gradient interactions (see Danish *et al.* (2016*b*)). The work of Wilczek & Meneveau (2014) is another successful example of using conditional means as input to a modelled stochastic process. Wilczek & Meneveau (2014) showed that the Fokker–Planck equation for the velocity-gradient PDF can be written in terms of conditional means. Currently, we are committed to making attempts to model the pressure Hessian tensor conditioned upon local topological and dilatation states in compressible turbulence. In compressible flows, potentially, there are far more possible topological states (Chong *et al.* 1990; Suman & Girimaji 2010) than those in incompressible flows. The conclusions from this study regarding the lifetimes of various topologies found in compressible turbulence provide a measure with which to judge which topologies are more persistent and long lasting than others. In the evolutionary history of a given particle, the more persistent topologies and their associated physics can be preferably targeted from a modelling point of view (rather than all those numerous topologies which are short lived and thus do not influence the velocity-gradient dynamics for long enough) to arrive at simple and robust models. Indeed, further details of such models require more research. However, the authors believe that this is a prospective way in which the findings of this study can be leveraged to arrive at improved models of compressible velocity-gradient dynamics.

7. Conclusions

We investigate the dynamics of velocity gradients in compressible decaying turbulence employing the Lagrangian approach of following a set of identified fluid particles. Well-resolved direct numerical simulations over a range of turbulent Mach number along with a well-validated Lagrangian particle tracker are employed for this study. We examine the invariants of the velocity-gradient tensor using the Lagrangian approach and compute lifetimes of various topologies in compressible turbulence. In particular, we identify the role of initial turbulent Mach number and

the normalised dilatation rate on topology lifetimes. Explanation of the identified trends is then provided in terms of the geometric constraint of the *p–q–r* space and the disparity in the speed of the fluid particles in the *p–q–r* space. Further, using our Lagrangian data and the associated analysis, we clearly demonstrate the limitation of the so-called conditional mean trajectory (CMT) in explaining certain aspects of the dynamics of velocity-gradient invariants. While the lifetimes computed with the Lagrangian trajectory are in complete agreement with the population composition of the entire flow field, the lifetimes computed by conditional mean trajectories show significant errors.

Acknowledgements

REFERENCES

ARMITAGE, P. J. 2010 *Astrophysics of Planet Formation*. Cambridge University Press.

ASHURST, W. T., CHEN, J. Y. & ROGERS, M. M. 1987*a* Pressure gradient alignment with strain rate and scalar gradient in simulated Navier–Stokes turbulence. *Phys. Fluids* **30** (10), 3293–3294.

ASHURST, W. T., KERSTEIN, A. R., KERR, R. M. & GIBSON, C. H. 1987*b* Alignment of vorticity and scalar gradient with strain rate in simulated Navier–Stokes turbulence. *Phys. Fluids* **30** (8), 2343–2353.

ATKINSON, C., CHUMAKOV, S., BERMEJO, M. I. & SORIA, J. 2012 Lagrangian evolution of the invariants of the velocity gradient tensor in a turbulent boundary layer. *Phys. Fluids* **24** (10), 105104.

BECHLARS, P. & SANDBERG, R. D. 2017*a* Evolution of the velocity gradient tensor invariant dynamics in a turbulent boundary layer. *J. Fluid Mech.* **815**, 223–242.

BECHLARS, P. & SANDBERG, R. D. 2017*b* Variation of enstrophy production and strain rotation relation in a turbulent boundary layer. *J. Fluid Mech.* **812**, 321–348.

BHATNAGAR, A., GUPTA, A., MITRA, D., PANDIT, R. & PERLEKAR, P. 2016 How long do particles spend in vortical regions in turbulent flows? *Phys. Rev.* E **94** (5), 1–8.

BIFERALE, L. & TOSCHI, F. 2005 Joint statistics of acceleration and vorticity in fully developed turbulence. *J. Turbul.* **6**, N40.

BUXTON, O. R. H. & GANAPATHISUBRAMANI, B. 2010 Amplification of enstrophy in the far field of an axisymmetric turbulent jet. *J. Fluid Mech.* **651**, 483502.

CANTWELL, B. J. 1992 Exact solution of a restricted Euler equation for the velocity gradient tensor. *Phys. Fluids* A **4** (4), 782–793.

CANTWELL, B. J. 1993 On the behavior of velocity gradient tensor invariants in direct numerical simulations of turbulence. *Phys. Fluids* A **5** (8), 2008–2013.

CANTWELL, B. J. & COLES, D. 1983 An experimental study of entrainment and transport in the turbulent near wake of a circular cylinder. *J. Fluid Mech.* **136**, 321–374.

CHEVILLARD, L. & MENEVEAU, C. 2006 Lagrangian dynamics and statistical geometric structure of turbulence. *Phys. Rev. Lett.* **97** (17), 174501.

CHEVILLARD, L. & MENEVEAU, C. 2011 Lagrangian time correlations of vorticity alignments in isotropic turbulence: observations and model predictions. *Phys. Fluids* **23** (10), 101704.

CHEVILLARD, L., MENEVEAU, C., BIFERALE, L. & TOSCHI, F. 2008 Modeling the pressure Hessian and viscous Laplacian in turbulence: comparisons with direct numerical simulation and implications on velocity gradient dynamics. *Phys. Fluids* **20** (10), 101504.

CHONG, M. S., PERRY, A. E. & CANTWELL, B. J. 1990 A general classification of three-dimensional flow fields. *Phys. Fluids* A **2** (5), 765–777.

CHU, Y. B. & LU, X. Y. 2013 Topological evolution in compressible turbulent boundary layers. *J. Fluid Mech.* **733**, 414–438.

DANISH, M., SINHA, S. S. & SRINIVASAN, B. 2016*a* Influence of compressibility on the lagrangian statistics of vorticity–strain-rate interactions. *Phys. Rev.* E **94** (1), 013101.

DANISH, M., SUMAN, S. & GIRIMAJI, S. S. 2016*b* Influence of flow topology and dilatation on scalar mixing in compressible turbulence. *J. Fluid Mech.* **793**, 633–655.

ELGHOBASHI, S. & TRUESDELL, G. C. 1992 Direct simulation of particle dispersion in a decaying isotropic turbulence. *J. Fluid Mech.* **242**, 655–700.

ELSINGA, G. E. & MARUSIC, I. 2010 Evolution and lifetimes of flow topology in a turbulent boundary layer. *Phys. Fluids* **22** (1), 015102.

FALKOVICH, G., FOUXON, A. & STEPANOV, M. G. 2002 Acceleration of rain initiation by cloud turbulence. *Nature* **419** (6903), 151.

GIRIMAJI, S. S. & POPE, S. B. 1990*a* A diffusion model for velocity gradients in turbulence. *Phys. Fluids* A **2** (2), 242–256.

GIRIMAJI, S. S. & POPE, S. B. 1990*b* Material-element deformation in isotropic turbulence. *J. Fluid Mech.* **220**, 427–458.

GIRIMAJI, S. S. & SPEZIALE, C. G. 1995 A modified restricted Euler equation for turbulent flows with mean velocity gradients. *Phys. Fluids* **7** (6), 1438–1446.

KERIMO, J. & GIRIMAJI, S. S. 2007 Boltzmann–BGK approach to simulating weakly compressible 3D turbulence: comparison between lattice Boltzmann and gas kinetic methods. *J. Turbul.* **8** (46), 1–16.

KUMAR, G., GIRIMAJI, S. S. & KERIMO, J. 2013 WENO-enhanced gas-kinetic scheme for direct simulations of compressible transition and turbulence. *J. Comput. Phys.* **234**, 499–523.

LIAO, W., PENG, Y. & LUO, L. S. 2009 Gas-kinetic schemes for direct numerical simulations of compressible homogeneous turbulence. *Phys. Rev.* E **80** (4), 046702.

LÜTHI, B., TSINOBER, A. & KINZELBACH, W. 2005 Lagrangian measurement of vorticity dynamics in turbulent flow. *J. Fluid Mech.* **528**, 87–118.

MARTÍN, J., OOI, A., CHONG, M. S. & SORIA, J. 1998 Dynamics of the velocity gradient tensor invariants in isotropic turbulence. *Phys. Fluids* **10**, 2336–2346.

MARTÍN, M. P., TAYLOR, E. M., WU, M. & WEIRS, V. G. 2006 A bandwidth-optimized WENO scheme for the effective direct numerical simulation of compressible turbulence. *J. Comput. Phys.* **220** (1), 270–289.

MENEVEAU, C. 2011 Lagrangian dynamics and models of the velocity gradient tensor in turbulent flows. *Annu. Rev. Fluid Mech.* **43**, 219–245.

OHKITANI, K. 1993 Eigenvalue problems in three-dimensional Euler flows. *Phys. Fluids* A **5** (10), 2570–2572.

O'NEILL, P. & SORIA, J. 2005 The relationship between the topological structures in turbulent flow and the distribution of a passive scalar with an imposed mean gradient. *Fluid Dyn. Res.* **36** (3), 107–120.

OOI, A., MARTIN, J., SORIA, J. & CHONG, M. S. 1999 A study of the evolution and characteristics of the invariants of the velocity-gradient tensor in isotropic turbulence. *J. Fluid Mech.* **381**, 141–174.

PARASHAR, N., SINHA, S. S., DANISH, M. & SRINIVASAN, B. 2017*a* Lagrangian investigations of vorticity dynamics in compressible turbulence. *Phys. Fluids* **29** (10), 105110.

PARASHAR, N., SINHA, S. S., SRINIVASAN, B. & MANISH, A. 2017*b* GPU-accelerated direct numerical simulations of decaying compressible turbulence employing a GKM–based solver. *Intl J. Numer. Meth. Fluids* **83** (10), 737–754.

PATER, I. D. & LISSAUER, J. J. 2015 *Planetary Sciences*. Cambridge University Press.

PINSKY, M. B. & KHAIN, A. P. 1997 Turbulence effects on droplet growth and size distribution in clouds-A review. *J. Aerosol Sci.* **28** (7), 1177–1214.

PIROZZOLI, S. & GRASSO, F. 2004 Direct numerical simulations of isotropic compressible turbulence: influence of compressibility on dynamics and structures. *Phys. Fluids* **16** (12), 4386–4407.

POPE, S. B. 2000 *Turbulent Flows*, pp. 483–489. Cambridge University Press.